nature communications

Article

https://doi.org/10.1038/s41467-026-74067-z

Tunable magnons in a dual-gated 2D antiferromagnet

Received: 2 June 2025

Accepted: 29 May 2026

Published online: 12 June 2026

Check for updates

Nele Stetzuhn[1,2] ✉, Abhijeet M. Kumar[1], Sviatoslav Kovalchuk[1], Denis Yagodkin[1], Louis Simon[1], Samuel Mañas-Valero[3,4], Eugenio Coronado[3], Takashi Taniguchi[5], Kenji Watanabe[5], Deepika Gill[2], Sangeeta Sharma[1,2], Piet W. Brouwer[1], Clemens von Korff Schmising[2], Stefan Eisebitt[2,6] & Kirill I. Bolotin[1,7]

The layered antiferromagnet CrSBr features magnons coupled to other quasiparticles, including excitons and polaritons, which enables their easy optical accessibility. In this work, we investigate the response of the magnons in few-layered devices to changes in carrier density and an applied perpendicular electric field. While the frequencies of both modes increase with the electron density, we reveal their asymmetric response with respect to the electric field. To understand the mechanism of this disparity, we propose a layer-resolved macrospin model describing the magnetic dynamics in thin, non-uniformly doped devices. Through this model we establish the dominant dependencies of the interlayer exchange interaction, magnetic anisotropy, and magnetic moment on the electron density and electric field in individual layers. We demonstrate an on-chip tunability of the in- and out-of-phase magnon frequencies by up to 2 GHz in a dual-gated trilayer device. Our results advance the applications of gate-tunable magnonic devices based on 2D materials.

Two-dimensional (anti)ferromagnets have garnered attention as an easily tunable platform to study static and ultrafast magnetism. Thin van der Waals magnets, like other two-dimensional materials, react strongly to external fields[1], strain[2–7], intercalation[8], and the formation of Moiré potentials[9–11], enabling reversible control of their magnetic properties. The semiconducting layered antiferromagnet CrSBr is of special interest due to its environmental stability[12–14] and strong anisotropy, stemming from its orthorhombic lattice structure[15]. This anisotropy results in monolayers of CrSBr being easy-axis ferromagnets along the crystallographic $\hat{b}$-axis, whereas neighboring layers couple antiferromagnetically below the Néel temperature of 132 K [16]. It also gives rise to a 1D character of the electronic band structure of CrSBr[15]. This, in turn, influences its transport properties[17,18] as well as the directionality of its tightly bound excitons[19,20].

Early studies on magnons in CrSBr have demonstrated their long coherence length[21], broadband tunability[2] and strong coupling to excitons[21–25]. In contrast to conventional antiferromagnets, in which magnetic order is often elusive to optical probes, this coupling allows one to observe magnon oscillations in absorption-based techniques at the excitonic[21,26] and polaritonic resonances[23]. The majority of studies on magnons in CrSBr have focused on bulk-like samples so far[21,27,28]. However, a new range of phenomena emerges in thin 2D magnets due to their sensitivity to external perturbations. For instance, the carrier density and electric field in few-layer samples, controlled by external gates, influence material properties such as the coercive field[29], critical temperature[30,31] and magnetic ground state[5,32]. While the effect of gating on magnon energies and transport has been studied in a few selected 2D magnetic systems[33–36], the response of the spin waves in thin CrSBr to electrostatic gating remains unexplored.

[1]Department of Physics, Freie Universität Berlin, Berlin, Germany. [2]Max Born Institute for Nonlinar Optics and Short-Pulse Spectroscopy, Berlin, Germany. [3]Instituto de Ciencia Molecular, Universidad de Valencia, Burjasot, Spain. [4]Department of Quantum Nanoscience, Kavli Institute of Nanoscience, Delft University of Technology, Delft, The Netherlands. [5]National Institute for Materials Science, Tsukuba, Japan. [6]Institut für Optik und Atomare Physik, Technische Universität Berlin, Berlin, Germany. [7]Halle-Berlin-Regensburg Cluster of Excellence CCE, Berlin, Germany. ✉e-mail: nele.stetzuhn@fu-berlin.de

https://doi.org/10.1038/s41467-026-74067-z

Indeed, characterizing the response of a dual-gated 2D antiferromagnet is challenging within the framework of current models: To describe magnetic excitations in bulk-like layered antiferromagnets, one commonly uses a macrospin model in which all spins within one layer are locked by the strong intralayer exchange interaction[37,38]. The complete antiferromagnetic bulk can then be described by only two coupled macrospins. In thin layered systems, however, an out-of-plane electric field leads to inhomogeneous doping across the device, breaking the symmetry between the layers. This leads to several questions about the detailed microscopic mechanisms governing magnon dynamics: How does the presence of free carriers affect the magnetic moment, interlayer exchange and magnetic anisotropies in CrSBr? What is the role of differing magnetic properties in individual layers as a result of electric-field-induced symmetry-breaking? Can a layer-resolved macrospin model describe the resulting magnonic behavior?

In this report, we address these questions by exploring the response of magnons in few-layer CrSBr devices to electrostatic gating. We find an opposing trend of the in- and out-of-phase magnon mode in response to an electric field in a dual-gated trilayer device, which, to the best of our knowledge, has not been reported previously. The detailed understanding of such a response is especially important in the context of developing spintronic applications of nanostructured 2D materials[39]. We therefore develop a minimal model connecting the layer-resolved charge carrier densities and electric fields to the magnetic properties of the sample. This allows us to explicitly correlate the measured magnon frequencies in CrSBr to its electrostatic properties using capacitive modeling and gate-dependent photoluminescence measurements.

Results

We utilize time-resolved (tr) reflectivity to investigate the gate-dependent behavior of magnons in CrSBr (see methods). The excitons in CrSBr exhibit a strong coupling to the magnetic order of the sample: Depending on the orientation of the macrospins in neighboring layers, the interlayer character and degree of localization of the excitons differs[40–42]. This results in a change of their binding energy, and accordingly their energetic resonance position in photoluminescence and reflectivity spectra[22,23,25]. Coherent magnons can therefore be seen as oscillations in the tr-reflectivity signal of the sample when probing close to an excitonic resonance[21,26,28].

The experimental platform to control electric field and doping consists of a thin CrSBr flake (2 − 8 layers, AFM in Supplementary Note 1) sandwiched between two graphite gates, each separated from the CrSBr by few-layered hBN (5 – 11 nm), as shown in Fig. 1a. The CrSBr is electrically grounded throughout the experiment, while the gate voltages V_b and V_t are separately applied to bottom and top graphite, respectively. In this scheme, the sum of gate voltages $V_b + V_t$ shifts the Fermi level in CrSBr, consequently changing its doping, while the difference between gate voltages $\Delta V = V_t - V_b$ controls the strength of a perpendicular electric field through the device. All measurements were performed at $T = 10$ K, well below the Néel temperature (temperature-dependent data in Supplementary Note 2). The magnons are excited with an ultrafast laser pulse tuned to the exciton or trion resonance at 1.376 eV or 1.350 eV, respectively. Subsequently, we probe the tr-reflectivity response at the same wavelength. We tune the pump- and probe energy to either resonance depending on the doping

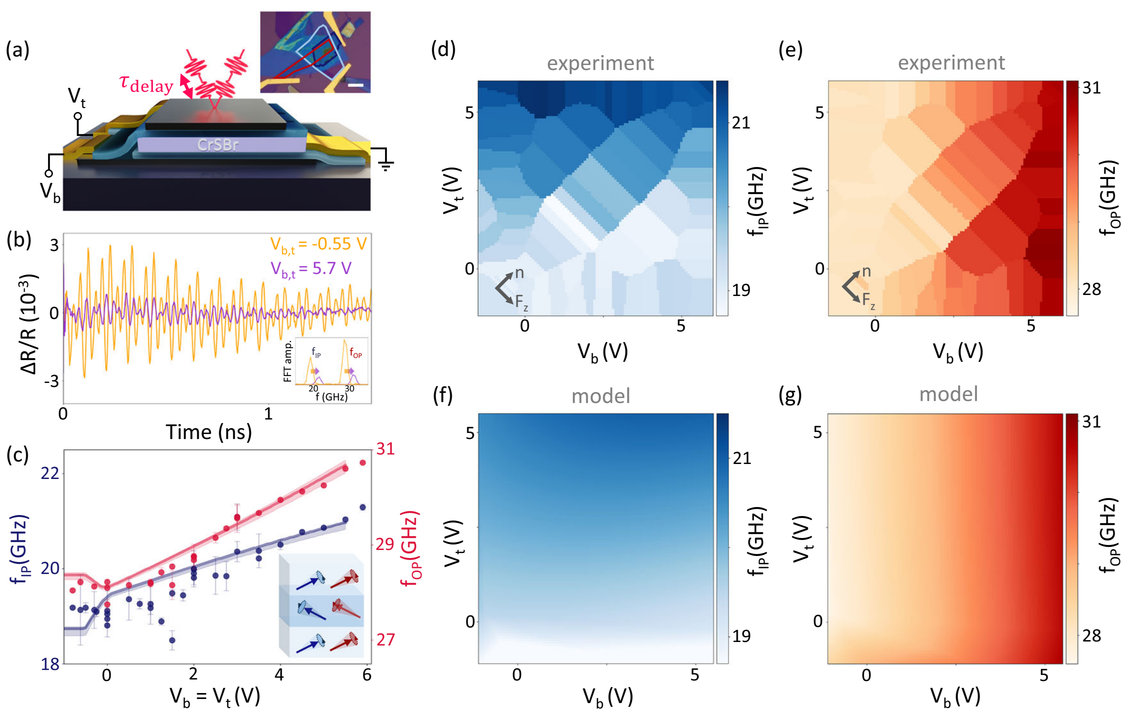

Fig. 1 | Magnons in dual-gated trilayer CrSBr. **a** Device scheme of a trilayer CrSBr flake (purple) encapsulated in hBN (light blue) with a top and bottom graphite gate (gray). The magnons are excited with an ultrafast pump laser pulse and read out by a probe pulse after τ_{delay}. The inset shows an optical image of the trilayer device (red: CrSBr flake, blue: top and bottom graphite), the scale bar corresponds to 10 µm. **b** Two exemplary time-resolved reflectivity traces after background subtraction, for weak ($V_b = V_t = -0.55$ V, orange) and strong ($V_b = V_t = 5.7$ V, violet) electron doping. The drop in signal intensity stems from the doping-dependent changes in the tr-reflectivity spectra (see Supplementary Fig. 3). An in-phase mode f_{IP} and an out-of-phase mode f_{OP} are extracted from the traces using a Fast Fourier Transform, shown in the inset. Electron doping shifts the magnon frequencies from 19.1 to 21.1 GHz and 28.1 to 30.8 GHz, respectively. **c** The complete doping response ($V_b = V_t$) of f_{IP} (blue, see inset) and f_{OP} (red, see inset) shows that the frequency increase starts after a threshold voltage. The errorbars are showing the uncertainty when extracting the peak position from the FFT. The solid lines are fits using the layer-resolved macrospin model. The shaded regions are calculated with the model using the errors of the fitting parameters given in the first row of Table 1. The complete V_b-V_t-dependencies of **d** f_{IP} and **e** f_{OP} plotted as Voronoi diagrams show a complex response to gating, which is opposite with electric field for the two modes (arrows indicate increasing electron density n and electric field F_z). Using a layer-dependent macrospin model connected to an electrostatic model we can reproduce the experimental trends in the fitted V_b-V_t-diagrams for both **f** f_{IP} and **g** f_{OP}.

 https://doi.org/10.1038/s41467-026-74067-z

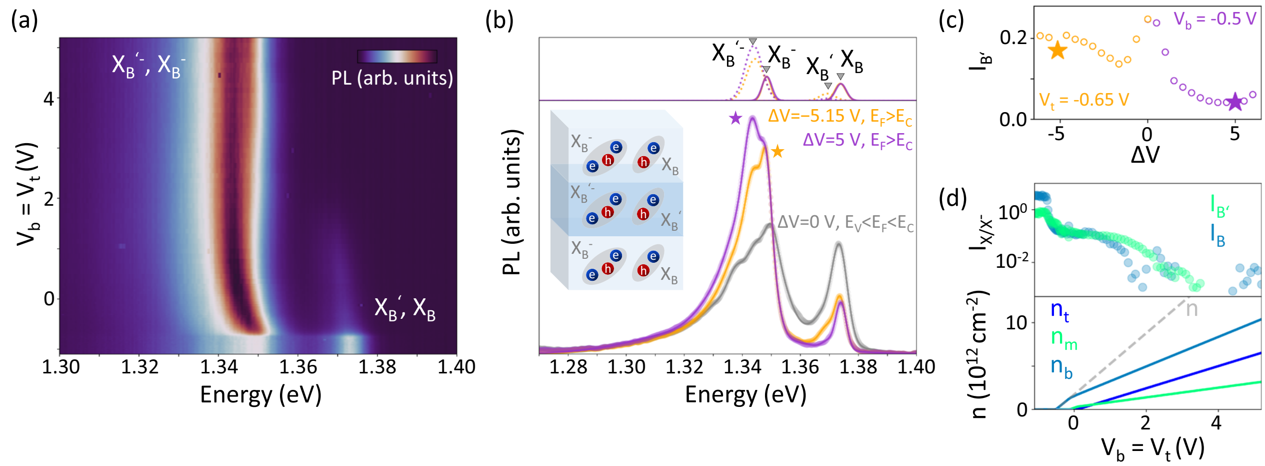

Fig. 2 | Dual-gate dependence of photoluminescence in trilayer CrSBr. a Doping-dependent PL map of the trilayer CrSBr showing the dimming of the neutral exitons X_B and X'_B around ~1.37 eV and brightening of the trions X_B^- and $X_B'^-$ at ~1.34 eV with increased electron density. **b** Exemplary PL spectra for undoped (gray) and doped (orange, purple) trilayer CrSBr (dots are datapoints, solid lines are fits using a sum of Gaussians). We assume a gate-independent background in the energy range between 1.32 and 1.34 eV to account for contributions of, e.g., X_A and phonon replicas of X_B in the fits. The upper panel shows the fitted exciton and trion peaks for the doped spectra. Both the exciton and trion peaks are split in two due to the complexes residing in the outer (B, solid lines) vs. the middle layer (B', dashed lines), as shown in the inset sketch. Under the same overall electron density n in the sample, but opposite electric field polarity $\propto \Delta V$ (orange: $\Delta V < 0$, purple: $\Delta V > 0$), the exciton-to-trion ratio I_B is almost identical (compare orange and purple solid exciton and trion fits in upper panel), while I'_B is sensitive to the field direction (compare orange and purple dashed exciton and trion fits in the upper panel). **c** Extracted I'_B for fixed $V_t = -0.65$ V (orange) or fixed $V_b = -0.5$ V (purple), but varying $\Delta V = V_t - V_b$ (spectra from (**b**) marked with stars). For the same doping level (graph is symmetric with doping), the ratio is lower for a positive ΔV, due to a higher electron density n_m for positive field direction. **d** Extracted doping-dependent exciton-to-trion ratios I_B and I'_B from (**a**) in the top panel, and layer-resolved carrier densities from electrostatic modeling in the lower panel. The drop of the exciton-to-trion ratios is closely followed by the modeled increase of n (gray).

level of the system to optimize the signal-to-noise ratio in the time-resolved reflectivity measurements. To enhance the signal strength, we apply a constant external magnetic field $H_0 \approx 0.1$ T using a permanent magnet in proximity of the sample (Supplementary Note 3).

First, we explore the effect of dual-gating in a trilayer of CrSBr. In Fig. 1b, we observe pronounced oscillations in the tr-reflectivity traces for different values of $V_b = V_t$ (orange: −0.55 V, purple: 5.7 V; exponential background subtracted from both). The oscillation amplitude decreases going from low (orange) to high (purple) gate voltages, as the spectral weight between exciton and trion resonance depends on the sample doping. The two oscillation frequencies around 19.1 ± 0.1 GHz and 28.1 ± 0.1 GHz ($V_b = V_t = -0.55$ V, inset of Fig. 1b) correspond to the in-phase and out-of-phase zero momentum magnon modes f_{IP} and f_{OP}, respectively, in accordance with previous reports[21,26,28,43]. As seen in Fig. 1c, increasing the gate voltages leads to an upshift of the frequencies of both modes, to a maximum of $f_{IP} = 21.1 \pm 0.1$ GHz and $f_{OP} = 30.8 \pm 0.1$ GHz ($V_b = V_t = 5.7$ V, inset of Fig. 1b). Notably, this shift is nonlinear – in particular, below $V_t = V_b \approx 1$ V, there is no significant change from the initial frequencies. In the complete V_b-V_t-dependence of f_{IP} and f_{OP} shown in Fig. 1d, e, we observe an asymmetry between the two modes in response to the perpendicular electric field F_z (arrows mark the direction of increase in doping n or field F_z). Specifically, f_{IP} increases mainly with V_t, while f_{OP} reacts to changes in V_b. In the following, we develop a microscopic picture to describe these dependencies.

To understand the mechanism behind the gate-dependent magnon frequencies, it is crucial to examine the carrier density configuration of our device. Generally, the ratio of intensities between neutral and charged excitons in gate-dependent photoluminescence (PL) measurements can be used as a proxy for carrier density in 2D materials[44–46]. In Fig. 2a, we plot the PL map of the trilayer CrSBr device as a function of gate voltage $V_b = V_t$ ($\Delta V = 0$). We see two main features in the energy ranges around 1.34 eV and 1.37 eV, which we assign to trions and excitons, respectively[47]. With increasing voltage, the intensity of the trion emission at 1.34 eV increases abruptly at $V_b = V_t \approx -0.8$ V, concurrently with a dimming of the excitonic peak at 1.37 eV. This is consistent with the neutral excitons binding to additional electrons, and suggests an intrinsic n-doping of our sample (as the trions dominate the spectrum at $V_b = V_t = 0$ V). Therefore, we conclude that below $V_b = V_t \approx -0.8$ V, the Fermi level lies in the bandgap and the sample is not significantly doped.

In Fig. 2b, the gray data points show an exemplary PL spectrum of the trilayer CrSBr device in this regime without applied field, i.e., $E_V < E_F < E_C$ (where E_V and E_C are the valence and conduction band energies, respectively), and $\Delta V = 0$ V. We observe strong emission at $X_B \approx 1.374$ eV with a shoulder at lower energies stemming from $X'_B \approx 1.370$ eV. In previous reports, X_B and X'_B were assigned to the excitonic transition between top valence and second lowest conduction band[15,22,47,48]. Their energetic splitting in samples with > 2 layers has been attributed to different dielectric screening in the outer (B) versus inner (B') layers, leading to a layer-resolved response of thin samples to electrostatic gating[47]. Around 1.34 eV, we find an amalgamation of several peaks even in the absence of trions (as $E_V < E_F < E_C$), which can be assigned to the X_A exciton (transition between top valence and bottom conduction band) and phonon replicas[15,22,47,48]. We note that a different interpretation of the emission at 1.34 and 1.37 eV has recently been given, in which the latter has been attributed to surface and the former to bulk excitons[49]. However, the thickness-dependent relative intensities of X_B and X'_B observed in our experiments support their assignment as excitons in the outer and inner layers (gate-dependent PL of samples with varying thickness in Supplementary Note 4).

For sufficiently high electron doping ($E_F > E_C$), we see emission from trions at $X_B^- \approx 1.348$ eV and $X_B'^- \approx 1.344$ eV (orange and purple spectra in Fig. 2b, fitted exciton and trion peaks in the upper panel). We note that the binding energies of the outer and inner layer trions $X_B^- - X_B = X_B'^- - X'_B = 26$ meV match, confirming the assignment of these peaks. Therefore, we use the relative intensities $I_B = \frac{I_{X_B}}{I_{X_B^-}}$ and $I_{B'} = \frac{I_{X'_B}}{I_{X_B'^-}}$ as indicators for the carrier densities of the outer layers, $n_t + n_b$, and the middle layer, n_m, respectively. Field-dependent measurements confirm this assignment: In Fig. 2b, we show two selected PL spectra for

 https://doi.org/10.1038/s41467-026-74067-z

opposite fields $F_z \propto \Delta V$, but equivalent doping level n (orange: $\Delta V < 0$, purple: $\Delta V > 0$). While the spectral weight I_B is nearly identical for the two (as either top or bottom layer become doped), $I_{B'}$ differs for $\Delta V > 0$ and $\Delta V < 0$ (compare the relative intensities of excitons and trions in the upper panel of Fig. 2b). Figure 2c shows the complete dependence of $I_{B'}$ on ΔV, in which the points at ΔV and $-\Delta V$ have roughly equivalent doping (full gate-dependence of I_B, $I_{B'}$ in Supplementary Note 4). Generally, the intensity $I_{B'}$ is smaller for positive than negative polarity of ΔV, which suggests a built-in electrical field $F_{z,0}$, possibly originating from surface charges[13].

We quantitatively link I_B and $I_{B'}$ to the layer-resolved electron densities n_i and electric fields $F_{z,ij}$ (where i, j = top, middle or bottom layer) using a simple electrostatic model[50,51]. For this, we assume that the interlayer character of the excitons is sufficiently small, because the weak applied external magnetic field only results in a small canting angle of the in-plane magnetization[42]. The main free parameters of the capacitive model are the built-in field $F_{z,0}$ and the carrier density n_0 at $V_b = V_t = 0$ V. The former leads to an offset between the bands of the neighboring layers, and the latter defines the initial position of the chemical potential. For the behavior of the layer-resolved carrier densities to resemble the experimentally obtained PL data, we arrive at $n_0 \approx 1.8 \times 10^{12}\,\mathrm{cm}^{-2}$ and $F_{z,0} \approx -0.02\,\mathrm{V\,nm}^{-1}$ (details of the model and gating maps of n_i and $F_{z,ij}$ in Supplementary Note 4). Comparing the resulting n_i as a function of $V_b = V_t$ (Fig. 2d, lower panel) to the ratios I_B and $I_{B'}$ extracted from Fig. 2a (Fig. 2d, upper panel), we find a reasonable alignment of the drop in both exciton-to-trion ratios around ~ −0.8 V with the onset of doping between ~− 0.5 and 0 V. The magnon frequencies in Fig. 1c follow the doping-dependence of the total carrier density of all three layers $n = \sum_i n_i$ (Fig. 2d bottom, gray dashed line) with a small offset in the gate voltage. This suggests that carrier-density induced modifications of magnetic properties contribute to the changes in magnon dynamics. However, the asymmetry with ΔV shown in the full gating maps of f_{IP} and f_{OP} in Fig. 1d, e cannot be explained by changes in n alone, indicating a dependence on the electric fields F_z, as well.

To explain how a gate-dependent layer asymmetry influences the magnonic behavior, we use a layer-resolved macrospin model. This approximation assumes strongly coupled spins within individual layers, such that their collective motion can be described by a single macrospin $\mathbf{m}_i$. Due to the long magnon lifetime (>900 ps) observed in Fig. 1b, and because we are mainly interested in the magnon frequencies, we omit damping effects. The dynamics of each macrospin are then governed by the layer-dependent effective field $\mathbf{H}_{\mathrm{eff},i}$ in the Landau–Lifshitz (LL) equation:

$$\frac{\mathrm{d}\mathbf{m}_i}{\mathrm{d}t} = -\gamma \mathbf{m}_i \times \mathbf{H}_{\mathrm{eff},i}. \quad (1)$$

Here, γ is the gyromagnetic ratio and $\mathbf{m}_i = M_{0,i}\hat{\mathbf{m}}_i$ is the layer-dependent macrospin. The effective field is given by

$$\mathbf{H}_{\mathrm{eff}_i} = -\nabla_{\mathbf{m}_i} E = \mathbf{H}_0 - \sum_{<i,j>} H_{\mathrm{E}_{ij}} \mathbf{m}_j + H_{\mathrm{a}_i} m_i^{\mathrm{a}} \hat{\mathbf{a}} + H_b m_i^{\mathrm{b}} \hat{\mathbf{b}}, \quad (2)$$

with the external field $\mathbf{H}_0$, the interlayer exchange coupling $H_{\mathrm{E}_{ij}}$ between neighboring layers i and j, and two anisotropies H_b and H_{a_i} along the easy $\hat{\mathbf{b}}$- and intermediate $\hat{\mathbf{a}}$-axis. The macrospin components m_i^{a} and m_i^{b} point in those same directions. In contrast to conventional models, the equilibrium macrospin, interlayer exchange and intermediate axis anisotropy are taken to be explicitly layer-dependent. To solve Eq. (1), the external field of $H_0 \approx 0.1$ T is taken to be purely in the out-of-plane direction. The excursions $\delta\mathbf{m}_i$ of the macrospins away from the equilibrium $\mathbf{m}_{i,0}$ are assumed small, allowing linearization of the LL equation. We then extract the magnon frequencies numerically.

To ensure the validity of the layer-resolved model, it is instructive to compare the numerical dispersion in the case of a bulk-like ($N = 100$ layers) sample to the analytical solution routinely used to model the bulk case (details in Supplementary Notes 5 and 6). In Fig. 3a, we show that the numerical model gives a low-frequency acoustic (blue points) and high-frequency optical (red points) magnonic branch consisting of bulk modes, in good agreement with the analytical results (solid line). The acoustic and optical modes at $k_z = 0$ correspond to f_{IP} and f_{OP}, and were excited and detected in previous pump-probe experiments[21]. Remarkably, two additional degenerate modes with low frequency emerge in the numerical model (marked gray in Fig. 3a). These are edge modes with an imaginary k_z, which decay exponentially into the bulk sample. They are a direct result of the open boundary conditions used (see Supplementary Fig. 11).

In thin samples, the magnon modes predicted by the layer-resolved model begin to deviate from those seen in the bulk. Figure 3b shows the magnon frequencies as a function of device thickness (expressed in layer number N). For $N > 10$, the eigenfrequencies of the bulk modes (between ~20 and 28 GHz) as well as the edge modes (below ~20 GHz) remain nearly thickness-independent, in agreement with previous experimental reports[21]. When reducing the layer number to $N < 10$, the maximum and minimum frequencies of the bulk modes start to deviate from the large N case. We assign this to the stronger influence of the edge layers, which experience a smaller interlayer exchange coupling. Additionally, the edge modes become non-degenerate and change their character, spreading across the whole sample instead of being localized at one side. In trilayers, we find that only the highest and lowest frequency magnons couple efficiently to a photothermal excitation, so we consider these modes as f_{OP} and f_{IP} in our experiments (extended discussion in Supplementary Note 7).

Having established the layer-resolved magnetic properties, we now turn to explaining the V_b-V_t-dependent behavior of f_{IP} and f_{OP} (Fig. 1d, e). In general, various physical processes can result in carrier-density or electric-field dependencies of the parameters in Eqs. (1) and (2) (Supplementary Note 8). To determine compatible mechanisms, we analyze the dependence of the magnon modes on overall changes in $M_0(=M_{0,\mathrm{t}}=M_{0,\mathrm{m}}=M_{0,\mathrm{b}})$, $H_\mathrm{a}(=H_{\mathrm{a}_\mathrm{t}}=H_{\mathrm{a}_\mathrm{m}}=H_{\mathrm{a}_\mathrm{b}})$ and $H_\mathrm{E}(=H_{\mathrm{E}_\mathrm{tm}}=H_{\mathrm{E}_\mathrm{mb}})$ in the numerical model within realistic ranges, see Fig. 3c–e. We observe that both f_{IP} and f_{OP} increase linearly with M_0 at similar rates (Fig. 3c). Both frequencies also increase with H_E, however at different rates, with a stronger influence on f_{OP} (Fig. 3d). Conversely, an increasing H_a leads to a decrease in both f_{IP} and f_{OP}, with a weaker effect on the latter (Fig. 3e). We only include one of the two anisotropies to be layer-dependent, as increasing H_a has a similar influence on the frequencies as decreasing H_b (Supplementary Fig. 10).

We now want to identify the dominating dependencies of $M_{0,i}$, $H_{a,i}$ and $H_{\mathrm{E}_{ij}}$ on n_i and $F_{z,ij}$ to reproduce the behavior in Fig. 1d, e. To this end, we compare different fitting approaches in Supplementary Note 9. From these considerations, we find that the experimentally observed shift of f_{IP} and f_{OP} at the same rate with respect to carrier density in Fig. 1c could be explained by a dependence of $M_{0,i}$ on n_i. In contrast, the asymmetric shifts of f_{IP} and f_{OP} vs. applied field in Fig. 1d, e point towards a competing field dependence of two parameters. Considering Fig. 3d, e, we suggest a linear dependence of both H_{a_i} and $H_{\mathrm{E}_{ij}}$ on $F_{z,ij}$. We therefore arrive at the following minimal set of dependencies:

$$H_{\mathrm{E}_{ij}} = H_{E_0} + \nu_\mathrm{E} F_{z,ij} \quad (3)$$

$$H_{\mathrm{a}_i} = H_{\mathrm{a}_0} + \nu_\mathrm{a} \sum_{\langle i,j \rangle} F_{z,ij} \quad (4)$$

$$M_{0,i} = 1 + \eta_\mathrm{M} n_i \quad (5)$$

 https://doi.org/10.1038/s41467-026-74067-z

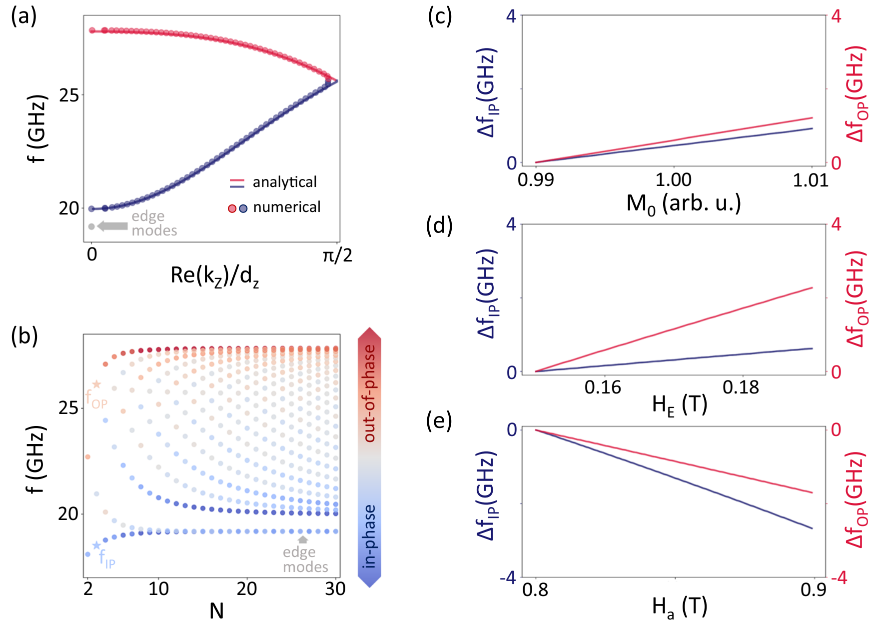

Fig. 3 | Layer-resolved macrospin model. a Comparison of the magnon dispersion of k_z ($k_x = k_y = 0$; d_z is interlayer spacing) calculated with the analytical bulk model (solid lines) and the layer-resolved numerical model for 100 layers (dots). Both models show an acoustic (blue) and an optical (red) magnon branch. The edge modes (gray) in the layer-resolved model are a result of the open boundary conditions. **b** Numerical magnon frequencies as a function of layer number N calculated with the layer-resolved model. The color-coding shows the efficiency of the coupling of the modes to in- or out-of-phase excitations (details in Supplementary Note 7). For high N, the degenerate edge modes lie ≈1 GHz below the bulk modes of the acoustic branch. For $N < 10$, the edge modes split. For $N = 3$, we identify the lowest and highest eigenvalues as the experimental f_{IP} and f_{OP}, respectively (marked by stars). Influence of changing the **c** length of the macrospin M_0, **d** interlayer exchange H_E, or **e** anisotropy H_a in all layers in the layer-resolved model. Both frequencies shift with M_0 at approximately the same rate, while their sensitivity to H_a and H_E differs. For all plots, the respective fixed parameters are $\gamma = 155\,\mathrm{GHz\,T^{-1}}$, $H_b = 1.3\,\mathrm{T}$, $H_a = 0.9\,\mathrm{T}$, and $H_E = 0.15\,\mathrm{T}$ (0.3 T in the analytical bulk model in (**a**)).

Table 1 | Macrospin model fit results for devices with different CrSBr thicknesses

thickness	H_{E_0} (T)	H_{a_0} (T)	H_b (T)	ν_a (T nmV^{-1})	ν_E (T nmV^{-1})	η_M (10^{-12} cm^2)
trilayer	0.163 ± 0.003	1.15 ± 0.2	1.48 ± 0.2	−0.86 ± 0.1	−0.85 ± 0.1	(7.3 ± 0.1) · 10^{-3}
bilayer 1	0.50 ± 0.01	0.98 ± 0.02	1.22 ± 0.01			
bilayer 2	0.67 ± 0.03	0.92 ± 0.02	1.16 ± 0.01			
5 layers	0.295 ± 0.005	0.96 ± 0.1	1.27 ± 0.01			
8 layers	0.25 ± 0.01	0.91 ± 0.01	1.16 ± 0.01			

This table summarizes the macrospin model fit parameters for a range of samples. The gyromagnetic ratio $\gamma = 155\,\mathrm{GHz\,T^{-1}}$ is fixed in the model. H_{E_0}, H_{a_0} and H_b are the internal fields in Eq. (2), and are fitted for each sample individually. The parameters ν_E and ν_a describe the electric-field dependencies of the exchange and anisotropy fields, respectively, and η_M is used to fit the doping-dependence of the layer macrospin, as described in Eqs. (3 to 5). We fitted all the parameters using the trilayer CrSBr data (resulting V_b-V_t-maps in Fig. 1f, g), with the results shown in the first row. To estimate the errors for the parameters found for the trilayer, the gyromagnetic ratio was varied within $\gamma = 155(15)\,\mathrm{GHz\,T^{-1}}$. For the 2-, 5-, and 8-layer CrSBr devices, the experimental frequencies were fitted to the macrospin model with ν_a, ν_E, and η_M fixed to the trilayer values in the top row. The resulting H_{a_0}, H_b and H_{E_0} differ slightly between samples. The errors of the free fit parameters of the 2-, 5-, and 8-layer results are estimated by varying ν_a, ν_E, and η_M within their error ranges.

where ν_E and ν_a are the fitting parameters we use to describe the electric-field dependencies of the interlayer exchange and anisotropy fields, respectively, and η_M is used to fit the doping-dependence of the layer macrospin. We fit the frequency gating maps in Fig. 1d, e to our layer-dependent LL model with Eqs. (3–5) using the n_i and $F_{z,ij}$ gating maps from the electrostatic model in Supplementary Fig. 6. The resulting fit parameters are summarized in the first row of Table 1. To estimate the error in the fit parameters of the trilayer data, we vary the fixed parameter $\gamma = 155(15)\,\mathrm{GHz\,T^{-1}}$ within the range of previously reported values[21]. In the doping-dependency of the modes in Fig. 1c, the model results (solid lines) show good agreement with the data, apart from slight deviations in the low carrier density regime. The modeled frequency maps shown in Fig. 1f, g also reproduce all basic trends of the experimental results reasonably well, in particular the opposing V_t- and V_b-sensitivity of the two magnon modes. To model this behavior, it is necessary to include the sign of the electric field in Eqs. (3) and (4)—which is surprising considering the symmetrical nature of the device stack.

The remaining discrepancies between modeled and experimental results stem from the sheer complexity of possible doping- and electric-field-related effects on magnetic properties. First, the position of the chemical potential—controlled by n—affects the imbalance between the occupied spin-up and spin-down states, affecting the magnetic moment μ and, in turn, the length of the layer macrospin M_0[52]. In addition, an n-dependent increase of the Coulomb repulsion influences the antiferromagnetic exchange constant[47,53,54]. Second, the relative population of states derived from e_g to t_{2g} orbitals in one layer is affected by both chemical potential and external field. This leads to a corresponding dependence of both exchange[53–55] and anisotropy terms[14,56–58]. Third, a perpendicular electric field shifts the energy bands associated with different orbitals in neighboring layers with respect to each other, again influencing the exchange coupling parameter[59].

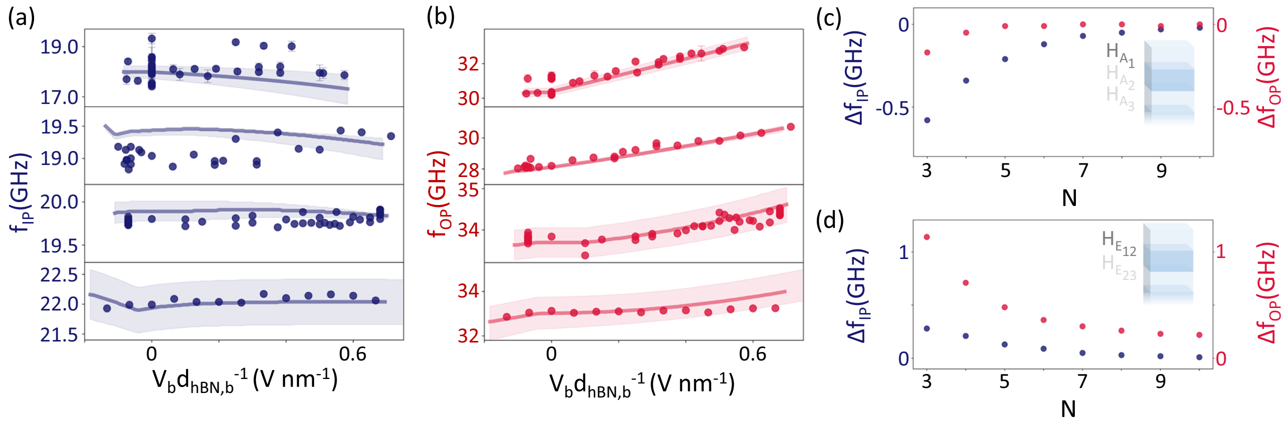

Fig. 4 | Thickness-dependence of magnon tunability. Comparison of the $\frac{V_b}{d_{hBN,b}}$-dependency of **a** f_{IP} and **b** f_{OP} for two, three, five, and eight layers of CrSBr. We scale the bottom gate voltage by the bottom hBN thickness $d_{hBN,b}$ for better comparability across the devices with different $d_{hBN,b}$. The solid lines and the shaded error regions show the frequencies fitted with the macrospin model (parameters in Table 1). In (**a**), f_{IP} is insensitive to the bottom gate across all devices, while the tunability of f_{OP} in (**b**) drops with layer number. Note the difference in frequency scales for better visibility of the small shift in the thick devices. **c** Modeled shifts Δf_{IP} and Δf_{OP} when changing H_{a_1} from 0.8 to 0.9 T (H_{a_i} of all other layers fixed to 0.9 T, H_b = 1.3 T, H_E = 0.15 T) as a function of layer number N. The shift drops to almost 0 for both modes in 10 layers. **d** Varying $H_{E_{12}}$ from 0.15 to 0.19 T (other exchange couplings fixed to 0.15 T, H_a = 0.8 T, H_b = 1.3 T) also results in smaller Δf_{IP} and Δf_{OP} for higher N.

We believe that the suggested dependencies in Eqs. (3) to (5) are the dominating mechanisms of the gate dependency of magnons in CrSBr. The inclusion of, e.g., additional terms such as $H_{E_{ij}} \propto n_i$, has not significantly improved the modeling of the experimental data. We also neglect any nonlinear or saturation effects. For the trilayer sample, we predict a change in $H_{E_{ij}}$ between neighboring layers of up to ~100 mT as a result of the applied electric field, while the tunability of H_{a_i} reaches almost ~200 mT. These changes of effective fields are an order of magnitude stronger than the previously reported gate-tunable internal field in a 10 nm thick $Cr_2Ge_2Te_6$ sample[35] and surpass the voltage-controlled magnetic anisotropy induced, for example, in CoFeB samples[58,60,61]. As $M_{0,i} \propto n_i$, the macrospin length changes most significantly in the bottom layer due to its strong doping, increasing by ~ 8% (complete gating maps of γ_i, H_{a_i}, $H_{E_{ij}}$ and discussion in Supplementary Note 9).

Additionally, the n_i- and $F_{z,ij}$-dependencies found for the trilayer predict the gate-dependent magnon frequency changes in samples of different thickness. The V_b-dependence of f_{IP} and f_{OP} in a 2, 5-, and 8-layer device, shown in comparison with the previous trilayer data, is plotted in Fig. 4a, b (additional data in Supplementary Note 10). In the bilayer device, we reach a similar tunability to that of the trilayer (in a dual-gated bilayer, we reach our maximum $\Delta f_{OP} \approx 4$ GHz, Supplementary Fig. 18). The magnitude of the gating effects decreases with thickness: In the 5-layer device, the maximum shift of f_{OP} is only 0.5 GHz, while the 8-layer device shows no discernible frequency shift. All devices also reproduce the insensitivity of f_{IP} to V_b observed in the trilayer. Using ν_a, ν_E, and η_M extracted from the trilayer data, we model the expected frequency shifts in the other devices. The fitted H_b, H_{a_0} and H_{E_0} differ from the trilayer results (values in Table 1, errors of the free fit parameters estimated by varying ν_a, ν_E and η_M within their error interval). The modeled gate-dependent changes (solid lines in Fig. 4a, b with shaded error regions) reproduce the data reasonably well, and agree with our experimental observations of reduced gate-sensitivity with higher layer number (see also Supplementary Fig. 17). In thicker devices, both carrier density and fields are induced mainly around the outer layers, with the inner ones being screened from the gates (electrostatic modeling for 2-, 5- and 8-layer device in Supplementary Note 4). The influence of these outer layers on the magnon frequencies decreases with increasing layer number N, illustrated in Fig. 4c, d. The magnon frequency shifts due to changes of the anisotropy (Fig. 4c) or interlayer exchange interaction (Fig. 4d) for one outer layer decrease drastically going from three to ten layers in the layer-resolved model.

Discussion

In summary, we have demonstrated the gate-tunability of the in- and out-of-phase magnon modes in trilayer CrSBr by up to 10 %. By using the contrasting response of the two magnons to the perpendicular electric field, their separate control is possible. We explain this gate-dependence in a Landau-Lifshitz model with layer-dependent magnetic moment, interlayer exchange, and anisotropy. By coupling the interlayer exchange and intermediate-axis anisotropy to the electric fields and the magnetic moment to the electron densities across layers, we arrive at a minimal model for our experimental results. The model explains most trends in the data, including the contrasting response of the two magnon modes to top and bottom gates, their doping response, as well as the observed thickness dependence. In particular, the gate-tunability of magnons in CrSBr drops from up to 4 GHz in a bilayer to ≈ 0.5 GHz in a 5-layer device, and vanishes for 8 layers.

The accuracy of the layer-resolved macrospin model is limited by several simplifications, mainly concerning the estimation of carrier density and electric field from PL measurements and the focus on the dominating linear dependencies of the magnetic sample parameters. In the future, we believe that experiments using a variable external magnetic field on CrSBr and other material systems, as well as studying higher-momentum magnons, can further improve our understanding of gate-dependent magnonic phenomena and expand our minimal model. Additionally, the magnon tunability could be increased by new gating techniques which surpass electrostatic gating in terms of the achievable doping and field[51,62,63]. Our findings open up new possibilities for using the on-chip control of magnons for magnonic circuits, e.g., for a phase shifter used in logic gates[39,64].

Methods

Sample fabrication and crystal growth

The crystals of CrSBr were synthesized by chemical vapor transport and subsequently characterized by X-ray diffraction, crystal diffraction (powder and single crystal), transmission electron microscopy, energy dispersive X-ray analysis, Raman and IR spectroscopy, superconducting quantum interference device magnetometry, and magneto-transport measurements, as reported in ref. 65.

The samples were fabricated using a dry-transfer technique after exfoliation on PDMS. The contacts were patterned by electron beam lithography followed by evaporation of 3 nm Cr and 80 nm Au.

Tr-reflectivity measurements

The tr-reflectivity measurements on the 3-, 5-, and 8-layer devices have been performed in a single-color pump and probe scheme. The laser source is a wavelength-tunable Ti:sapphire laser (Coherent Chameleon Ultra II, $\tau_{\mathrm{pulse}} \approx 140$ ps, $f_{\mathrm{rep}} = 80$ MHz). We spatially separate pump and probe beams before entering a reflective objective (Thorlabs LMM40x-P01) and focusing on the sample, into spot sizes of $d_{\mathrm{probe}} \approx 1\,\mu$m, $d_{\mathrm{pump}} \approx 3\,\mu$m. Thanks to the spatial separation of the reflected beams, we then filter out the pump beam using an iris. On the bilayer devices, we employed a two-color pump and probe scheme. For this, we used a high pump energy of 1.9 eV and probed around 1.67 eV, which is a higher-energy excitonic resonance of CrSBr[48]. We then filtered out the pump light using a lowpass filter in the detection path. In both configurations, the probe light is measured with a home-built photodetector (Hamamatsu photodiodes) using a lock-in amplifier synced to a chopper in the pump beam ($f = 2.1$ kHz). More details are provided in Supplementary Note 3.

PL measurements

All PL measurements were conducted using a continuous wave laser with an excitation wavelength of 670 nm and a laser power of 25 μW. The incoming laser light was linearly polarized along the $\hat{b}$-axis of the CrSBr flake. A refractive objective (Olympus LMPlanFL N 50x/0.50) focused the laser to a spot size of ≈1 μm. The resulting copolarized PL was captured with the Kymera 193i Spectrograph.

Dielectric constant of CrSBr

The dielectric constant of CrSBr used in the electrostatic model was calculated using Hubbard-corrected DFT energy functionals (LDA+U). The complete dielectric function is shown in Supplementary Fig. 5.

Data availability

The source data for this manuscript and its supplementary information is available in the Zenodo database under accession code https://doi.org/10.5281/zenodo.18982552.

References

1. Kim, D., Lee, C., Jang, B. G., Kim, K. & Shim, J. H. Drastic change of magnetic anisotropy in Fe_3GeTe_2 and Fe_4GeTe_2 monolayers under electric field studied by density functional theory. *Sci. Rep.* **11**, 17567 (2021).
2. Diederich, G. M. et al. Tunable interaction between excitons and hybridized magnons in a layered semiconductor. *Nat. Nanotechnol.* **18**, 23–28 (2022).
3. Esteras, D. L., Rybakov, A., Ruiz, A. M. & Baldoví, J. J. Magnon straintronics in the 2D van der Waals ferromagnet CrSBr from first-principles. *Nano Lett.* **22**, 8771–8778 (2022).
4. Pizzochero, M. & Yazyev, O. V. Inducing magnetic phase transitions in monolayer CrI_3 via lattice deformations. *J. Phys. Chem. C.* **124**, 7585–7590 (2020).
5. Ren, W. et al. Tunable electronic structure and magnetic anisotropy in bilayer ferromagnetic semiconductor $Cr_2Ge_2Te_6$. *Sci. Rep.* **11**, 1–9 (2021).
6. Hu, X. et al. Enhanced ferromagnetism and tunable magnetism in Fe_3GeTe_2 monolayer by strain engineering. *ACS Appl. Mater. Interfaces* **12**, 26367–26373 (2020).
7. Cenker, J. et al. Reversible strain-induced magnetic phase transition in a van der Waals magnet. *Nat. Nanotechnol.* **17**, 256–261 (2022).
8. Deng, Y. et al. Gate-tunable room-temperature ferromagnetism in two-dimensional Fe_3GeTe_2. *Nature* **563**, 94–99 (2018).
9. Xu, Y. et al. Coexisting ferromagnetic-antiferromagnetic state in twisted bilayer CrI_3. *Nat. Nanotechnol.* **17**, 143–147 (2021).
10. Wang, C., Gao, Y., Lv, H., Xu, X. & Xiao, D. Stacking domain wall magnons in twisted van der Waals magnets. *Phys. Rev. Lett.* **125**, 247201 (2020).
11. Tong, Q., Liu, F., Xiao, J. & Yao, W. Skyrmions in the Moiré of van der Waals 2D magnets. *Nano Lett.* **18**, 7194–7199 (2018).
12. Telford, E. J. et al. Layered antiferromagnetism induces large negative magnetoresistance in the van der Waals semiconductor CrSBr. *Adv. Mater.* **32**, 2003240 (2020).
13. Torres, K. et al. Probing defects and spin-phonon coupling in CrSBr via resonant Raman scattering. *Adv. Funct. Mater.* **33**, 2211366 (2023).
14. Ziebel, M. E. et al. CrSBr: An air-stable, two-dimensional magnetic semiconductor. *Nano Lett.* **24**, 4319–4329 (2024).
15. Klein, J. et al. The bulk van der Waals layered magnet CrSBr is a quasi-1D material. *ACS Nano* **17**, 5316–5328 (2023).
16. López-Paz, S. A. et al. Dynamic magnetic crossover at the origin of the hidden-order in van der Waals antiferromagnet CrSBr. *Nat. Commun.* **13**, 1–10 (2022).
17. Wu, F. et al. Quasi-1D electronic transport in a 2D magnetic semiconductor. *Adv. Mater.* **34**, 2109759 (2022).
18. Telford, E. J. et al. Coupling between magnetic order and charge transport in a two-dimensional magnetic semiconductor. *Nat. Mater.* **21**, 754–760 (2022).
19. Smolenski, S. et al. Large exciton binding energy in a bulk van der Waals magnet from quasi-1D electronic localization. *Nat. Commun.* **16**, 1134 (2025).
20. Liebich, M. et al. Controlling Coulomb correlations and fine structure of quasi-one-dimensional excitons by magnetic order. *Nat. Mater.* **24**, 384–390 (2025).
21. Bae, Y. J. et al. Exciton-coupled coherent magnons in a 2D semiconductor. *Nature* **609**, 282–286 (2022).
22. Wilson, N. P. et al. Interlayer electronic coupling on demand in a 2D magnetic semiconductor. *Nat. Mater.* **20**, 1657–1662 (2021).
23. Dirnberger, F. et al. Magneto-optics in a van der Waals magnet tuned by self-hybridized polaritons. *Nature* **620**, 533–537 (2023).
24. Wang, T. et al. Magnetically-dressed CrSBr exciton-polaritons in ultrastrong coupling regime. *Nat. Commun.* **14**, 1–7 (2023).
25. Brennan, N. J., Noble, C. A., Tang, J., Ziebel, M. E. & Bae, Y. J. Important elements of spin-exciton and magnon-exciton coupling. *ACS Phys. Chem. Au*. **4**, 322–327 (2024).
26. Sun, Y. et al. Dipolar spin wave packet transport in a van der Waals antiferromagnet. *Nat. Phys.* **20**, 794–800 (2024).
27. Dirnberger, F. et al. Spin-correlated exciton-polaritons in a van der Waals magnet. *Nat. Nanotechnol.* **17**, 1060–1064 (2022).
28. Bae, Y. J. et al. Transient magnetoelastic coupling in CrSBr. *Phys. Rev. B* **109**, 104401 (2024).
29. Jiang, S., Li, L., Wang, Z., Mak, K. F. & Shan, J. Controlling magnetism in 2D CrI_3 by electrostatic doping. *Nat. Nanotechnol.* **13**, 549–553 (2018).
30. Wang, H., Fan, F., Zhu, S. & Wu, H. Doping enhanced ferromagnetism and induced half-metallicity in CrI_3 monolayer. *EPL*. **114**, 47001 (2016).
31. Wang, H., Qi, J. & Qian, X. Electrically tunable high Curie temperature two-dimensional ferromagnetism in van der Waals layered crystals. *Appl. Phys. Lett.* **117**, 83102 (2020).
32. Huang, B. et al. Electrical control of 2D magnetism in bilayer CrI_3. *Nat. Nanotechnol.* **13**, 544–548 (2018).
33. Zhang, X.-X. et al. Gate-tunable spin waves in antiferromagnetic atomic bilayers. *Nat. Mater.* **19**, 838–842 (2020).
34. Qi, S. et al. Giant electrically tunable magnon transport anisotropy in a van der Waals antiferromagnetic insulator. *Nat. Commun.* **14**, 1–8 (2023).

35. Hendriks, F., Rojas-Lopez, R. R., Koopmans, B. & Guimarães, M. H. D. Electric control of optically-induced magnetization dynamics in a van der Waals ferromagnetic semiconductor. *Nat. Commun.* **15**, 1–9 (2024).
36. de Wal, D. K., Mena, R. L., Zohaib, M. & van Wees, B. J. Gate control of magnon spin transport in unconventional magnon transistors based on the van der Waals antiferromagnet $CrPS_4$. *Phys. Rev. B* **110**, 224434 (2024).
37. Gurevich, A.G. & Melkov, G. A. *Magnetization Oscillations and Waves* (CRC Press, 1996).
38. Rezende, S. M., Azevedo, A. & Rodríguez-Suárez, R. L. Introduction to antiferromagnetic magnons. *J. Appl. Phys.* **126**, 151101 (2019).
39. Chumak, A. V., Vasyuchka, V. I., Serga, A. A. & Hillebrands, B. Magnon spintronics. *Nat. Phys.* **11**, 453–461 (2015).
40. Śmiertka, M. et al. Distinct magneto-optical response of Frenkel and Wannier excitons in CrSBr. *Nat. Commun.* **17**, 1777 (2026).
41. Kalitukha, I. V. et al. Magnetic switching of exciton lifetime in CrSBr. Preprint at *arXiv* https://doi.org/10.48550/arXiv.2601.05413 (2026).
42. Heißenbüttel, M. C. et al. Quadratic optical response to a magnetic field in the layered magnet CrSBr. *Phys. Rev. B* **111**, 075107 (2025).
43. Cham, T. M. J. et al. Anisotropic gigahertz antiferromagnetic resonances of the easy-axis van der Waals antiferromagnet CrSBr. *Nano Lett.* **22**, 6716–6723 (2022).
44. Mak, K. F. et al. Tightly bound trions in monolayer MoS_2. *Nat. Mater.* **12**, 207–211 (2012).
45. Mouri, S., Miyauchi, Y. & Matsuda, K. Tunable photoluminescence of monolayer MoS_2 via chemical doping. *Nano Lett.* **13**, 5944–5948 (2013).
46. Ross, J. S. et al. Electrical control of neutral and charged excitons in a monolayer semiconductor. *Nat. Commun.* **4**, 1–6 (2013).
47. Tabataba-Vakili, F. et al. Doping-control of excitons and magnetism in few-layer CrSBr. *Nat. Commun.* **15**, 4735 (2024).
48. Lin, K. et al. Probing the band splitting near the Γ point in the van der Waals magnetic semiconductor CrSBr. *J. Phys. Chem. Lett.* **15**, 6010–6016 (2024).
49. Shao, Y. et al. Magnetically confined surface and bulk excitons in a layered antiferromagnet. *Nat. Mater.* **24**, 391–398 (2025).
50. Pisoni, R. et al. Absence of interlayer tunnel coupling of K-valley electrons in bilayer MoS_2. *Phys. Rev. Lett.* **123**, 117702 (2019).
51. Kovalchuk, S. et al. Revealing hidden interlayer excitons in 2D bilayers via hybrid molecular gating. *Nat. Commun.* **16**, 9893 (2025).
52. Han, R., Xue, X. & Li, P. Enhanced ferromagnetism, perpendicular magnetic anisotropy and high Curie temperature in the van der Waals semiconductor CrSeBr through strain and doping. *Phys. Chem. Chem. Phys.* **26**, 12219–12230 (2024).
53. Kugel, K. I. & Khomskii, D. I. Crystal structure and magnetic properties of substances with orbital degeneracy. *Zh. Eksp. Teor. Fiz.* **64**, 1429–1439 (1973).
54. Kugel, K. I. & Khomskii, D. I. The Jahn-Teller effect and magnetism: transition metal compounds. *Sov. Phys. - Uspekhi* **25**, 621–641 (1982).
55. Mazurenko, V. V., Mila, F. & Anisimov, V. I. Electronic structure and exchange interactions of $Na_2V_3O_7$. *Phys. Rev. B* **73**, 014418 (2006).
56. Maruyama, T. et al. Large voltage-induced magnetic anisotropy change in a few atomic layers of iron. *Nat. Nanotechnol.* **4**, 158–161 (2009).
57. He, K. H., Chen, J. S. & Feng, Y. P. First principles study of the electric field effect on magnetization and magnetic anisotropy of FeCo/MgO(001) thin film. *Appl. Phys. Lett.* **99**, 72503 (2011).
58. Rana, B. et al. Electric field control of spin waves in ultrathin CoFeB films. *Phys. Rev. B* **100**, 224412 (2019).
59. Wang, Y., Luo, N., Zeng, J., Tang, L. M. & Chen, K. Q. Magnetic anisotropy and electric field induced magnetic phase transition in the van der Waals antiferromagnet CrSBr. *Phys. Rev. B* **108**, 054401 (2023).
60. Li, X. et al. Enhancement of voltage-controlled magnetic anisotropy through precise control of Mg insertion thickness at CoFeB|MgO interface. *Appl. Phys. Lett.* **110**, 52401 (2017).
61. Nozaki, T. et al. Voltage-induced magnetic anisotropy changes in an ultrathin FeB layer sandwiched between two MgO layers. *Appl. Phys. Express* **6**, 073005 (2013).
62. Weintrub, B. I. et al. Generating intense electric fields in 2D materials by dual ionic gating. *Nat. Commun.* **13**, 1–6 (2022).
63. Domaretskiy, D. et al. Quenching the bandgap of two-dimensional semiconductors with a perpendicular electric field. *Nat. Nanotechnol.* **17**, 1078–1083 (2022).
64. Rana, B. & Otani, Y. Voltage-controlled reconfigurable spin-wave nanochannels and logic devices. *Phys. Rev. Appl.* **9**, 014033 (2018).
65. Boix-Constant, C. et al. Probing the spin dimensionality in single-layer CrSBr van der Waals heterostructures by magneto-transport measurements. *Adv. Mater.* **34**, 2204940 (2022).

Acknowledgements

We thank T. Kampfrath and G. Woltersdorf for useful discussions. We thank B. Höfer for technical support.

Author contributions

N.S. and K.I.B. conceived the project. A.M.K. and D.Y. designed the experimental setup. N.S. and S.K. prepared the samples. N.S. performed the measurements. S.K. provided the original code for electrostatic modeling. N.S., L.S., K.I.B., and P.B. developed the layer-resolved macrospin model. N.S. performed the electrostatic and macrospin modeling of the results. N.S. analyzed the data. S.M.V. and E.C. grew the CrSBr crystals. T.T. and K.W. grew the hBN crystals. D.G. and S.S. performed the DFT calculations of the dielectric function. K.I.B., C.K.S., and S.E. supervised the project. N.S. and K.I.B. wrote the manuscript with input from all co-authors.

Funding

We acknowledge the German Research Foundation (DFG) for financial support through the Collaborative Research Center TRR 227 Ultrafast Spin Dynamics projects B08, B03 and A04, as well as the priority programme SPP2244. We acknowledge additional funding by the German Research Foundation (DFG) as part of the German Excellence Strategy - EXC3112/1 - 533767171 (Center for Chiral Electronics) and SfB1772 (Heterostructures of Molecules and 2D materials). Open Access funding enabled and organized by Projekt DEAL.

Competing interests

The authors declare no competing interests.

Additional information

Supplementary information The online version contains supplementary material available at https://doi.org/10.1038/s41467-026-74067-z.

Correspondence and requests for materials should be addressed to Nele Stetzuhn.

Peer review information *Nature Communications* thanks Jun-Feng Dai, Akashdeep Kamra, Yang Li, and the other anonymous reviewer(s) for their contribution to the peer review of this work. A peer review file is available.